PROCEEDINGS A

royalsocietypublishing.org/journal/rspa

Research

Cite this article: Birnbaum J, Lev E, Llewellin EW. 2021 Rheology of three-phase suspensions determined via dam-break experiments. *Proc. R. Soc. A* **477**: 20210394.
https://doi.org/10.1098/rspa.2021.0394

Received: 10 May 2021
Accepted: 19 August 2021

Subject Areas:
fluid mechanics, materials science, volcanology

Keywords:
three phase, bubble suspension, rheology, analogue experiments, lava flows

Author for correspondence:
Janine Birnbaum
e-mail: janineb@ldeo.columbia.edu

Rheology of three-phase suspensions determined via dam-break experiments

Janine Birnbaum[1], Einat Lev[1] and Ed W. Llewellin[2]

[1]Lamont-Doherty Earth Observatory, Columbia University, 61 Rte. 9w, Palisades, NY 10964, USA
[2]Department of Earth Sciences, Durham University, Durham DH1 3LE, UK

JB, 0000-0003-0873-2989; EL, 0000-0002-8174-0558; EWL, 0000-0003-2165-7426

Three-phase suspensions, of liquid that suspends dispersed solid particles and gas bubbles, are common in both natural and industrial settings. Their rheology is poorly constrained, particularly for high total suspended fractions ($\gtrsim$0.5). We use a dam-break consistometer to characterize the rheology of suspensions of (Newtonian) corn syrup, plastic particles and CO_2 bubbles. The study is motivated by a desire to understand the rheology of magma and lava. Our experiments are scaled to the volcanic system: they are conducted in the non-Brownian, non-inertial regime; bubble capillary number is varied across unity; and bubble and particle fractions are $0 \leq \phi_{gas} \leq 0.82$ and $0 \leq \phi_{solid} \leq 0.37$, respectively. We measure flow-front velocity and invert for a Herschel–Bulkley rheology model as a function of ϕ_{gas}, ϕ_{solid}, and the capillary number. We find a stronger increase in relative viscosity with increasing ϕ_{gas} in the low to intermediate capillary number regime than predicted by existing theory, and find both shear-thinning and shear-thickening effects, depending on the capillary number. We apply our model to the existing community code for lava flow emplacement, PyFLOWGO, and predict increased viscosity and decreased velocity compared with current rheological models, suggesting existing models may not adequately account for the role of bubbles in stiffening lavas.

1. Introduction

Two-phase liquid–solid (particle) and liquid–gas (bubble) suspensions are important across nature and industry.

Electronic supplementary material is available online at https://doi.org/10.6084/m9.figshare.c.5627134.

THE ROYAL SOCIETY PUBLISHING

Consequently, their behaviour has been well characterized: see Mader *et al.* [1] for a thorough review. Numerous studies show that the apparent viscosity of particle suspensions increases with particle volume fraction, and intermediate and concentrated suspensions show non-Newtonian behaviour with finite yield stresses and strain-rate dependence [2–4]. Bubble suspensions exhibit an increase or decrease in apparent viscosity relative to the liquid phase. Concentrated bubble suspensions also show non-Newtonian behaviour, including non-zero yield stresses and shear-thinning or shear-thickening behaviour [5–15]. A key parameter determining the rheology of bubble suspensions is the capillary number

$$\mathrm{Ca} = \frac{\mu a \dot{\gamma}}{\Gamma}, \tag{1.1}$$

where μ is the liquid viscosity, a is the undeformed bubble radius, $\dot{\gamma}$ is the shear strain rate and Γ is the surface tension. The capillary number reflects the ratio of viscous stresses that deform bubbles and capillary stresses that restore them [7,13,14]. When $\mathrm{Ca} \gg 1$, viscous stress dominates, bubbles deform easily and decrease relative viscosity; when $\mathrm{Ca} \ll 1$, the surface tension resisting bubble deformation dominates, bubbles remain nearly spherical and increase relative viscosity.

The rheology of three-phase suspensions (liquid suspending particles and bubbles) has received much less detailed investigation, but is known to be a complex function of the suspended phase fractions, micro-textural properties such as the size and shape distributions of particles and bubbles, and the conditions of shear [10,16,17]. The only systematic experimental study, which was limited to $\phi_{\mathrm{solid}} \lesssim 0.5$, $\phi_{\mathrm{gas}} \lesssim 0.3$ and low capillary number [17], found that the rheology was well described by a simple convolution of existing two-phase rheology models in which the liquid and bubbles were treated as an effective medium that suspended the particles. We expect that interactions between bubbles and particles will become increasingly important at higher bubble and particle fractions such that a simple convolution of two-phase models is insufficient.

Magma (and lava, which is its subaerial counterpart) is a natural three-phase suspension, composed of a molten silicate liquid (melt) that suspends a variable fraction of solid particles (crystals) and gas bubbles. The suspending melt is Newtonian over a wide range of strain rates, and has a viscosity that can vary over orders of magnitude [18,19]. Bubble and crystal volume fractions can both range from 0 to 1, and typically change, along with melt viscosity, during transport through the Earth's crust and over its surface. The rheology of magma exerts a first-order control on the dynamics of its eruption, and the emplacement of subsequent lava flows [20,21]. Whilst the rheology of natural magmas has been measured directly [22–25], such measurements are challenging to perform and interpret, and are not well suited to systematic investigation of parameter space. As a result, it has been common for the rheology of magmatic suspensions to be investigated via analogue experiments [4,6,13,17,26]. Even with the use of analogues, it has proven challenging to perform rheometry on samples with $\phi_{\mathrm{gas}} \gtrsim 0.5$. This is because samples with a high bubble fraction are difficult to prepare, particularly when the sample also contains particles, and because they are prone to breakdown when loaded into a conventional rheometer. We conduct experiments in which bubbles are grown *in situ* via a chemical reaction, and analysed using a dam-break consistometer. This approach circumvents both problems, allowing us to investigate samples with bubble fractions ($0 \leq \phi_{\mathrm{gas}} \leq 0.8$) and particle fractions ($0 \leq \phi_{\mathrm{solid}} \leq 0.37$) that span the most relevant ranges for natural magma and lava.

2. Theoretical background

(a) Scaling

We scale our analogue suspensions to basaltic magma, which typically has a pure-melt viscosity in the range 10^2 to 10^4 Pas ($10^3 - 10^5$ Poise) at eruption temperature [19], and surface tension between 0.05 and 0.3 N m^{-1} [27–29]. Bubbles that nucleate deep within the volcanic plumbing system are likely to be small (radius $\sim 10^{-5}$ to 10^{-3} m) and experience very low shear rates

($\sim 10^{-10}$ to $10^{-5}\,s^{-1}$), resulting in capillary numbers $Ca \ll 1$ [30,31]. As magmas decompress on their way to the surface, bubbles grow and coalesce to radii $\sim 10^{-5} - 10^{-2}$ m or larger [32–34]. However, decimeter-sized bubbles often segregate from the flow, making a suspension rheology approach no longer appropriate. Magma in basaltic dikes experiences strain rates up to $\sim 10^{1}$ to $10^{2}\,s^{-1}$ [35] and the capillary number therefore spans from $Ca \ll 1$ to $Ca \gg 1$. At the surface, lava flows, particularly fast-moving flows (velocities ~ 1 m s^{-1}) may experience strain rates of 10^{-3} to $10^{2}\,s^{-1}$, and both high and low capillary numbers [8]. The viscosity of silicate melts is sufficiently high that viscous stresses at the particle scale dominate over inertial and Brownian stresses [4]. We therefore conduct experiments that span from low to high capillary number, while remaining in the non-inertial, non-Brownian regimes.

(b) Theoretical framework for rheology of three-phase suspensions

To our knowledge, the only theoretically grounded model for the rheology of three-phase suspensions is that of Phan-Thien & Pham [16]. They present a model for the effective Newtonian viscosity, η, of a three-phase suspension of the form

$$\eta_{r,s} = \frac{\eta}{\mu} = \eta_{r,p}\,\eta_{r,b}, \tag{2.1}$$

where $\eta_{r,s}$ is the relative viscosity of the three-phase suspension (i.e. suspension viscosity normalized by the liquid viscosity), and $\eta_{r,p}$ and $\eta_{r,b}$ are the relative viscosities of the two-phase components (particle-liquid, and bubble-liquid suspensions, respectively). Importantly, this relation treats one two-phase system as an effective viscous medium in which the third phase is suspended. Truby *et al.* [17] validated this theoretical form against experimental data, using existing models for the viscosity of the two-phase suspensions

$$\eta_{r,p} = \left(1 - \frac{\phi_{\text{solid}}}{\phi_m}\right)^{-B_{\text{solid}}} \quad \text{and} \quad \eta_{r,b} = (1 - \phi_{\text{gas}})^{-B_{\text{gas}}}, \tag{2.2}$$

following, respectively, Mueller *et al.* [4] and Llewellin & Manga [7], where Einstein exponents $B_{\text{solid}} = 2$ and $B_{\text{gas}} = 1$, and ϕ_m is a maximum packing fraction of solid particles. Both Phan-Thien & Pham [16] and Truby *et al.* [17] note that the definition of ϕ_{gas} and ϕ_{solid} depends on which two-phase suspension is chosen as the effective medium; in this study we choose the particle suspension such that $\phi_{\text{solid}} = V_{\text{solid}}/(V_{\text{solid}} + V_{\text{liquid}})$ and $\phi_{\text{gas}} = V_{\text{gas}}/(V_{\text{gas}} + V_{\text{solid}} + V_{\text{liquid}})$, where V denotes the volume of the subscript phase.

Truby *et al.* [17] extend the model of Phan-Thien & Pham [16] to allow for non-Newtonian effects by equating the suspension viscosity, η, with the consistency, K, in the Herschel–Bulkley model [36]:

$$\tau = \tau_y + K\dot{\gamma}^n, \tag{2.3}$$

where τ is the shear stress, τ_y is the yield stress and n is the flow index ($n > 1$ implies shear-thickening, $n < 1$ shear-thinning). We adopt this approach in the analysis below.

3. Methods

(a) Experimental set-up

Our experiments use a Bostwick (dam-break) consistometer, in which fluid is released from a reservoir into a confined rectangular channel (figure 1). The reservoir measures 20 cm along the length of the channel, and the channel extends another 1 m; the reservoir and channel have a constant width of 15 cm. The reservoir can be filled to a maximum depth of 15 cm, and in our experiments the initial reservoir depth ranges from 4 to 13 cm. The walls of the consistometer are transparent to allow observation and imaging of the flow. We use 42DE corn syrup diluted to a 77% sugar concentration, measured using a Brix refractometer. Corn syrup is a Newtonian fluid with a viscosity that depends on water-content (dilution) and temperature. Our experiments are

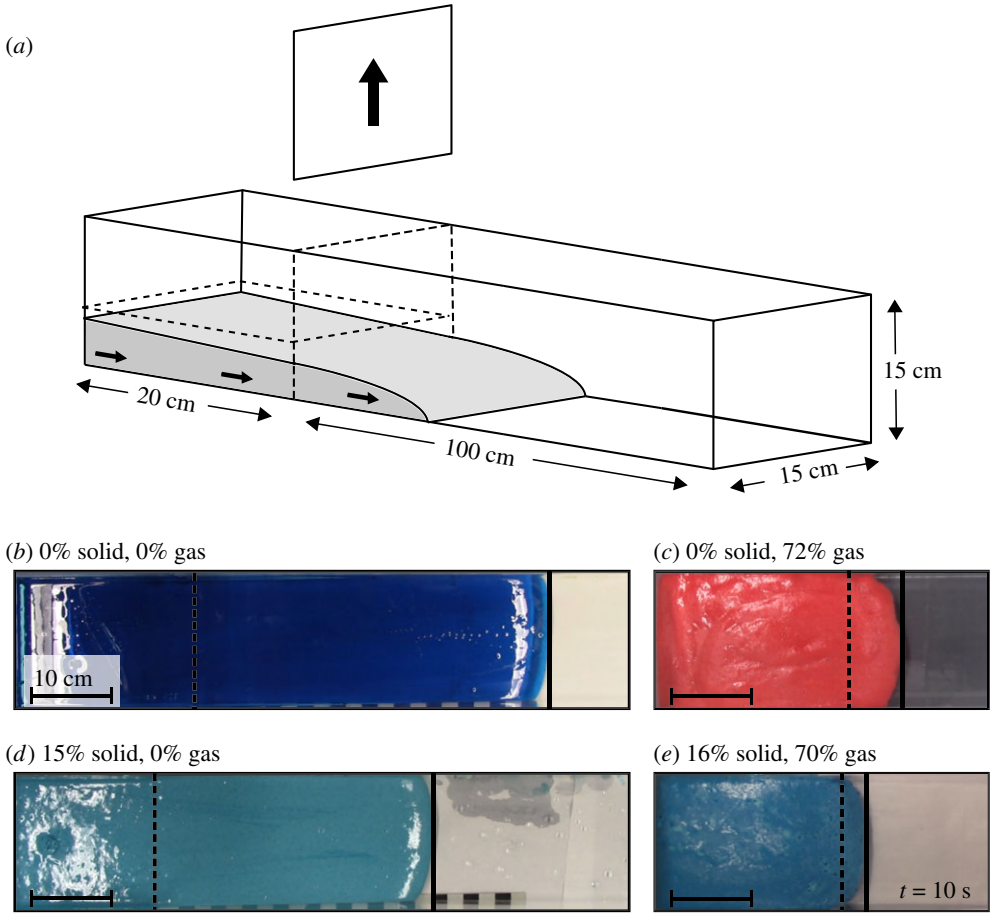

Figure 1. (*a*) Dam-break set-up showing fluid release into a confined channel. (*b–e*) Top views contrasting the slower flow-front progression with the addition of particles and bubbles, with starting position (dashed) and position 10 s after dam removal (solid). All photos have the same scale. (Online version in colour.)

conducted at room temperature (isothermal for a given experiment), which varied between 18.1 and 30.5°C, corresponding to syrup viscosities in the range $13.3 \geq \mu \geq 3.73$ Pa s, measured using a Brookfield rotational viscometer. The surface tension of corn syrup is $\Gamma = 0.08$ N m^{-1} [37]; the surface tension of sugar solutions is only weakly dependent on concentration [38].

To the syrup, we add rigid plastic particles sieved to a mesh size of 60–80 (sourced from Precise Finishing Inc Stock No. GP-PP60/80, Polyplus / Type II). Particles have near-neutral buoyancy ($\rho_{\text{syrup}} = 1395$ kg m^{-3}, $\rho_{\text{plastic}} = 1370$ kg m^{-3}), are angular and slightly elongate (aspect ratio 1.5 to 2), and have a dominantly unimodal size distribution (long axis ≈ 200 to 400 µm). Particles are stirred into the suspension by hand, which leads to minimal air entrapment, as shown in the microphotograph in the electronic supplementary material, figure S2. The volume fraction of solids in the suspension is determined prior to the introduction of gas by mass of syrup and particles (uncertainty of 1–2 volume %). When multiple experiments with the same particle content were performed, a large volume of syrup and particles was prepared, but gas was introduced to each sample individually.

Gas is introduced via a chemical reaction between baking soda ($NaHCO_3$) and citric acid ($C_6H_8O_7$), which produces water vapour and CO_2 gas. Reactants are added with a $\sim 3:4$ ratio by mass, yielding an empirical relation of roughly 0.5 g baking soda and 0.7 g citric acid per 100 g syrup, per 10% desired gas volume fraction. The reaction begins immediately and the sample is

allowed to rise for approximately 20 min prior to its release into the confined channel. Samples with $\phi_{gas} < 0.6$ are risen in a separate container, then transferred to the consistometer reservoir; samples with $\phi_{gas} > 0.6$ are more delicate, and are risen in the reservoir to avoid foam disruption during transfer. Final gas volume fraction is calculated from the final mixture density. Mass of the suspension is measured when transferring to the channel and the volume is calculated using the internal channel dimensions and the height of the mixture within the reservoir as measured through the channel walls. This method leads to ~ 3 to 5% relative uncertainty on the volume and resultant approximately 3 to 5% relative uncertainty on the density and an absolute uncertainty of approximately 0.02 to 0.04 on ϕ_{gas}.

The water vapour that forms during the reaction is insufficient to lower the syrup viscosity appreciably. In the experiments with the highest concentration of reactants (9 g total per 100 g of syrup), water could, in principle, result in a dilution from 77% to 76.6% sugar if all the water dissolved, which would change the viscosity from 7.6 Pas (76 Poise) to 6.5 Pas (65 Poise) at 23°C. However, a test suspension, from which the evolved gas was allowed to escape overnight showed no additional dissolved water when analysed using the Brix refractometer.

The flow begins with the removal of the dam, which takes less than 1 s. The dam is typically coated with approximately 2 to 3 mm of syrup, when removed, effectively shortening the length of the fluid in the reservoir. However, in this geometry, propagation is insensitive to the length of the reservoir and this is below the spatial resolution of our forward model. Flow progression along the channel is recorded by time-lapse photographs from the side at a rate of 1 frame-per-second (FPS), and from above using a video camera (30 FPS). Experiments last between 15 and 180 s, with most 30 to 90 s in duration. We process the top-view videos to extract the flow front position over time. In the tracking algorithm, the video, rotated to align the flow direction left to right, is processed by manually identifying the starting position, scale and centre line in each video, and setting an appropriate threshold on the brightness of the red, blue or green channel of the image to distinguish syrup from the background. In some cases, the time-distance profile of the flow front was smoothed to remove artefacts caused by the flash from the side-view camera. The flow front position is compared with a forward model of dam-break flow to invert for the rheological parameters.

(b) Extracting rheological parameters from experiments

We follow the derivations of Liu & Mei [39] and Balmforth *et al.* [40] for time evolution of flow thickness, h, of a Herschel–Bulkley fluid flowing down a slope:

$$\frac{\partial h}{\partial t} = \frac{\partial}{\partial x}\left[\left(\frac{\rho g}{K}\right)^{1/n} \frac{n|\sin\theta - (\partial h/\partial x)\cos\theta|^{1/n-1} Y^{1/n+1}}{(n+1)(2n+1)}((2n+1)h - nY)\left(\sin\theta - \frac{\partial h}{\partial x}\cos\theta\right)\right] \tag{3.1a}$$

and

$$Y = h - \frac{\tau_y}{\rho g|\sin\theta - (\partial h/\partial x)\cos\theta|}, \tag{3.1b}$$

where x is the along-channel distance, ρ is the fluid density, g is the acceleration due to gravity and θ is the channel slope.

This forward model is valid for non-inertial laminar flow of a gravitationally settling fluid experiencing no-slip conditions at the base of the flow and no-stress at the free surface. In the inertial regime, propagation of the flow front would be expected to scale with the shallow water speed $\sqrt{gH}$. Based on the short-time similarity solution of the flow front position given by Balmforth *et al.* [40] for a Newtonian fluid, $X \sim 0.2845\hat{t}^{1/2}$, for $t = (L/H)(KL/\rho g H^2)^{1/n}\hat{t}$ and $x = L\hat{x}$, where L is the reservoir length and H the reservoir depth, we expect inertia would be dominant for $t \lesssim 10^{-5} - 10^{-2}$ s, which is much shorter than the duration of our experiments. We confirm that all experiments are in the laminar regime by verifying that the Reynolds number, Re, is below the cutoff for the onset of turbulence at Re ~ 1000. We calculate Re for a free surface flow of a Herschel–Bulkley fluid in a rectangular channel as Re =

$\rho\bar{u}^{2-n}D^n/((\tau_y/8)(D/\bar{u})^n + K((3m+1)/(4m))^n 8^{n-1})$, $m = nK(8\bar{u}/D)^n/(\tau_y + K(8\bar{u}/D)^n)$ [41], where $\bar{u}$ is the mean velocity, D is the hydrodynamic radius, $D = 4HW/(2H+W)$, for channel width $W = 15$ cm and channel depth $H \sim h$. We find Reynolds numbers $\lesssim 10$, well below the cutoff. We confirm no-slip conditions via imaging through the base of the channel, which shows that bubbles are well coupled to the base (electronic supplementary material, figure S3). We neglect the effect of surface tension between the syrup and air, which becomes important for $h < 2\sqrt{\Gamma/\rho g} \approx 0.5$ cm [42]. Accordingly, we restrict our experiments to have a starting reservoir volume $H > 4$ cm. Finally, we require that the suspension be able to deform under its own weight, which requires that the Bingham number, $B < 1$, where $B \equiv \tau_y L/\rho g H^2$ [40]. We prepared a suspension of $\phi_{\text{solid}} = 0.46$, and find that for a flow height of 2.5 cm, it does not deform under its own weight, suggesting that yield stress must exceed 42 Pa.

We solve equation (3.1*a*) numerically using a finite-difference scheme on a centred three-point stencil that is second-order accurate in space and we use two-step Runge–Kutte for second-order accuracy in time. Initial conditions are fluid height $h = H$, where $x \leq L$ (within the reservoir) and $h = 0$ elsewhere. Boundary conditions are no-slip on the bottom, no-stress at the free surface, $\partial h/\partial x|_{x=x_L} = 0$ (no inflow on low slope) and $h|_{x=x_R} = 0$, where x_R is chosen to be sufficiently far from the final position of the flow front such that flow does not reach the far boundary (domain length is 20% longer than the final experimental flow length). The domain is discretized in space evenly with 52 grid points and with a constant time step of $\Delta t = 6.67 \times 10^{-4}$ s. The forward model assumes that temperature, rheology and density of the fluid are constant in time and space. We allow slope to be non-zero in the model solution to account for sensitivity of flow advance rate to slope angles below our uncertainty for direct measurement ($\leq 0.5^\circ$). We extract the position of the flow front over time from the model by identifying where $h \approx 0$, below a threshold of 1×10^{-4} to account for numerical diffusion, smoothed linearly between grid points in x.

We use the evolution of the flow front over time in the experiments as a constraining observation in our inversion for rheological parameters. We invert for rheological parameters (K, τ_y, n) and the slope (θ) using an Ensemble Kalman Filter (EnKF) approach [43,44]. This is a probabilistic approach in which the forward model is instantiated many times with varying parameters that are modified iteratively to minimize the misfit between the model and data (typically approx. 2000 data points). All samples are propagated together between iterations, which allows faster convergence than a random walk. We use Gaussian priors centred about a visually determined close fit for the rheological parameters, and about zero for the slope. Standard deviations were 10%, 10%, 5% and 1° for the initial distributions of K, τ_y, n and θ, respectively. EnKF simulations are initialized with 300 samples and run for five iterations; convergence is typically achieved within four iterations, insensitive to small changes in the initial parameters (electronic supplementary material, figure S5). In other Earth-science applications, EnKF is often used to update probabilities by assimilating more information through time, for example in volcano monitoring [43,44]. We do not use this capability of EnKF; all information about the flow progression is included from the beginning. We use the Python implementation of the EnKF algorithm provided on GitHub by geoyanzhan3[1] [43,44]. We report the numerically determined maximum-likelihood value, and uncertainty given by the 5% and 95% quantiles. We find uncertainty values of $\lesssim 20\%$ in K, $\lesssim 20\%$ in τ_y and $\lesssim 10\%$ in n.

4. Results

We present results from 35 dam-break experiments spanning $0 \leq \phi_{\text{solid}} \leq 0.37$ and $0 \leq \phi_{\text{gas}} \leq 0.82$ (figure 2; electronic supplementary material, table 1). We find that, with increasing volume fraction of solids, relative consistency ($K_r = K/\mu$) increases, yield stress increases, and flow index decreases (more shear-thinning), consistent with previous studies [1]. Increasing gas fraction in all cases increases relative consistency and yield stress. Gas-bearing experiments show both

[1]See https://github.com/geoyanzhan3/EnKF_tutorial

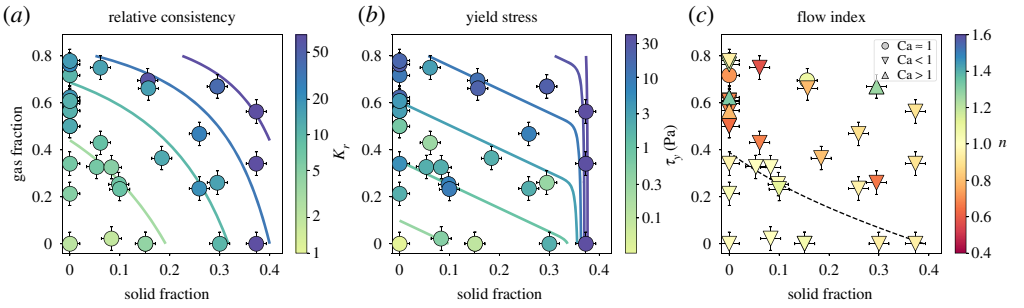

Figure 2. Experimental rheology measurements plotted against solid (*x*-axis) and gas (*y*-axis) volume fractions, and the value of (*a*) relative consistency, K, and (*b*) yield stress, τ_y shown in colour. Contours represent the best-fitting empirical models on the same colour scale. In panel (*c*), colour represents the maximum capillary number, Ca, and flow index, n, indicated by marker shape. The dashed black line indicates the critical volume fraction for the onset of shear-rate dependent behaviour below which flow is shear-rate-independent, and above which shear-thinning behaviour is expected at intermediate and low Ca and shear-thickening behaviour is predicted for high Ca. Data are reported in electronic supplementary material, table 1. (Online version in colour.)

shear-thinning ($n < 1$) and shear-thickening ($n > 1$) behaviour, with increasing n correlated with increasing Ca.

We use our measurements to parameterize the model framework presented in §2b, and find empirical expressions for K_r, τ_y and n as functions of phase volume fractions and (where relevant) the maximum capillary number. We calculate the maximum capillary number using equation (1.1) with the maximum observed bubble size from each experiment (0.5 to 8.2 mm) and estimate the maximum strain rate from experiment videos. Best fitting parameter values for these empirical models are determined using the L-BFGS-B algorithm for limited-memory, quasi-Newton, bound-constrained optimization [45] implemented in Python; uncertainty is estimated from the approximated Hessian matrix.

We find the following empirical relationships:

$$K_r = \left(1 - \frac{\phi_{\text{solid}}}{\phi_m}\right)^{-B_{\text{solid}}} (1 - \phi_{\text{gas}})^{-B_{\text{gas}}}, \tag{4.1a}$$

$$\tau_y = 10^{C_1(\phi_{\text{solid}} - \phi_{c,\tau_y})} + 10^{C_2(\phi_{\text{solid}} + \phi_{\text{gas}} - \phi_{c,\tau_y})} \tag{4.1b}$$

and

$$n = \begin{cases} 1, & \phi_{\text{solid}}(1 - \phi_{\text{gas}}) + \phi_{\text{gas}} \le \phi_{c,n} \\ 1 + (C_3 - C_4\text{Ca})(\phi_{c,n} - \phi_{\text{solid}}(1 - \phi_{\text{gas}}) - \phi_{\text{gas}}), & \phi_{\text{solid}}(1 - \phi_{\text{gas}}) + \phi_{\text{gas}} > \phi_{c,n} \end{cases} \tag{4.1c}$$

where $\phi_m = 0.56 \pm 0.20$, $B_{\text{solid}} = 2.74 \pm 1.56$ and $B_{\text{gas}} = 1.98 \pm 0.09$, $C_1 = 80.0 \pm 10.9$, $C_2 = 1.98 \pm 0.23$, the critical volume fraction for the onset of appreciable yield stress $\phi_{c,\tau_y} = 0.35 \pm 0.01$, $C_3 = 0.70 \pm 0.25$, $C_4 = 0.55 \pm 0.31$, and the critical volume fraction for the onset of shear rate dependence $\phi_{c,n} = 0.39 \pm 0.12$. Results from each experiment are plotted in figure 2 and compared with contours for the best-fitting model plotted on the same colour scale. Misfits between the experiments and model are given in electronic supplementary material, table 1.

5. Discussion

(a) Comparison with previous studies

(i) Relative consistency, K_r

Our expression for consistency (equation (4.1*a*)) has the functional form presented in equation (2.1), such that it can be decomposed into separate functions for the two-phase components,

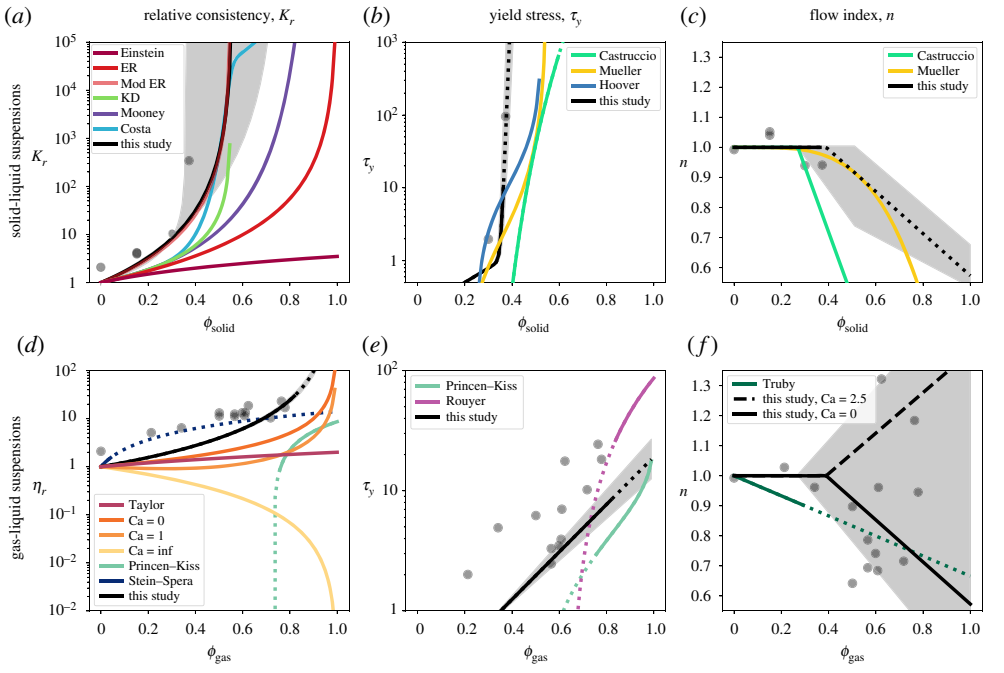

Figure 3. Comparison between popular rheology models and the model proposed in this study. (*a* and *d*) show relative consistency, (*b* and *e*) yield stress, and (*c* and *f*) flow index in the two-phase end-member cases of (*a–c*) solid–liquid only and (*d–f*) gas–liquid only suspensions. Best-fit models for our experiments are plotted in black, with grey shaded regions highlighting model uncertainties. ER = Roscoe [46], KD = Krieger & Dougherty [3]; also see Mooney [47], Costa *et al.* [48], Taylor [15], Llewellin & Manga [7], Princen & Kiss [11], Stein & Spera [14], Castruccio *et al.* [26], Mueller *et al.* [4], Hoover *et al.* [49], Rouyer *et al.* [12], Truby *et al.* [17] (electronic supplementary material, table 1). Dotted lines indicate extrapolations outside the calibration region for experimental studies. Grey markers are our two-phase experiments. Note that the model is constrained on the three-phase dataset so does not necessarily pass through this subset of the experiments. (Online version in colour.)

facilitating comparison with previous studies (figure 3*a*,*d*, equations and parameters in electronic supplementary material, table 1). For particle suspensions ($\phi_{gas} = 0$), we find a $K_r(\phi_{solid})$ dependence that has the same functional form as that of Krieger & Dougherty [3] and Roscoe [46]. We do not have experiments for $\phi_{solid} > 0.37$, where relative consistency rapidly increases and a transition to another functional form, such as that in Costa *et al.* [48], may be appropriate. For bubble suspensions ($\phi_{solid} = 0$), we find a $K_r(\phi_{gas})$ dependence that is stronger than most previous studies, with bubbles having a stronger stiffening effect on the suspensions. Furthermore, we find that in our experiments, bubbles always increase the relative consistency, regardless of capillary number, in contrast to previous studies [6,13].

We note that our consistency model (equation (4.1*a*)) is optimized against the full three-phase dataset, hence three-phase interactions are likely to play a role in these discrepancies with models that are fitted against two-phase data. For instance, breakup of bubbles between interacting particles, and the formation of liquid-film bridges between particles may both amplify the effect of the bubble fraction on suspension rheology, and cause the rheology to be controlled by the smallest bubbles, which are in the low Ca regime, despite observations of deformation in the largest bubbles (electronic supplementary material, figure S2), which imply $\mathrm{Ca} \gg 1$ locally.

(ii) Yield stress, τ_y

We select an empirical exponential-type relationship for yield stress (equation (4.1*b*)), which overlaps with previous two-phase studies (figure 3*b* and 3*e*). We observe a much stronger effect

of particles compared to gas, but onset at around the same volume fraction. Yield stresses we observe in three-phase suspensions are higher than would be predicted by a linear superposition of the two-phase components, indicating again that interactions among the phases are important. At intermediate volume fractions, we find moderately good agreement with Hoover *et al.* [49] and Mueller *et al.* [4]. The gas–liquid suspension experiments compare favourably with results by Princen & Kiss [11] and Rouyer *et al.* [12], although there is limited overlap between regions of calibration.

(iii) Flow index, n

We fit flow index data using a piecewise continuous linear relationship after Castruccio *et al.* [26] and Truby *et al.* [17]. For particle suspensions, and for bubble suspensions at low Ca, this formulation yields a shear-thinning behaviour, which is consistent with previous relationships (figure 3*c*,*f*). With increasing Ca and gas fraction, it transitions to shear-thickening, a behaviour reported in previous studies [10].

(b) Data limitations

We use the dam-break consistometer set-up to measure the rheology of three-phase suspensions in order to avoid bubble breakdown, which is common in conventional rheometers. This set-up allows us to attain high bubble volume fractions, but requires numerical inversion and additional considerations for direct comparison with rheometry data collected via other methods. The behaviour of Herschel–Bulkley fluids in confined channels and on unconfined slopes has been investigated theoretically and experimentally [50], primarily using kaolin clay suspensions and Carbopol, which show variable agreement with measurements collected in conventional rheometers. Most studies that use channel flow to investigate rheology use the approach to a final runout state [51], the height profile [52–54], the internal velocity [55–58], or the runout distance with time [40,52,59,60]. The internal velocity and height profiles observed in experiments using kaolin clay typically compare favourably with theory, except during the initial slumping stage, in which inertia is dominant, and near the flow front where significant curvature requires more sophisticated modelling [53,58]. By contrast, experiments using Carbopol show systematic offsets compared with conventional rheometers, possibly a result of basal slip, three-dimensional effects such as levee formation [55,56], or a scale effect introduced in the narrow gap of conventional rheometers compared with a relatively large microstructural length scale in Carbopol [58]. Our results use the runout distance with time to measure rheology, which shows good agreement with conventional rheometry for experiments on corn syrup, xanthan gum and kaolin suspensions [40]. We expect our suspensions to behave similarly to two-phase kaolin particle suspensions, and further verify that basal slip and levee formation do not occur in our experiments. Given findings in previous work on two-phase suspensions in dam-break experiments and the good agreement between our experiments and existing particle-bearing suspensions, we do not expect systematic offsets in the rheometric parameters determined in our study compared with what would be measured in a conventional rheometer.

Our forward model is one-dimensional (depth-integrated) and cannot capture any effects perpendicular to the channel direction. Visual inspection of the experiments suggests that there is not pronounced cross-channel flow. Our channel width, at 15 cm, is larger that used by Balmforth *et al.* [40], who find a 10 cm channel outperforms a 5 cm channel. We estimate the boundary layer width for a Herschel–Bulkley fluid, $\delta = ((1 + 1/n)^n K U^n H/\tau_y)^{n/(n+1)}$ [61] at high Bingham number ($\mathrm{Bi} = \tau_y/K(U/\delta)^{-n}$), where U is the maximum velocity along the channel, and scales with the height of the flow at low Bingham number. Our experiments fall in the intermediate Bingham number range, and we expect boundary layer thicknesses between less than 1 and 17.5 cm. Experiments with boundary layers larger than half the channel width (8.5 cm) are noted in electronic supplementary material, table 1. The misfits between these experiments and the

model do not show systematic differences, nor are the misfits different in magnitude compared with experiments with low predicted boundary layer thicknesses.

The uncertainties on the values for K_r, τ_y and n we derive from inversion of the experimental data are 25%, 31% and 14%, respectively, and the mismatch with models for those parameters (equations (4.1*a*)–(4.1*c*)) are 35%, 106% and 10%. Our experiments show good repeatability at $\phi_{\text{gas}} \leq 0.6$. If we compare experiments for which ϕ_{solid} and ϕ_{gas} are within ±5%, and de-trended K_r, τ_y and n values using their respective models, we find ranges of 38%, 149% and 20% in those parameters, which are of the same order as uncertainties and mismatch. For $\phi_{\text{gas}} > 0.6$, the data show greater variability with ranges of 68%, 154% and 73%, respectively. Data variability may be related to experimental sources of uncertainty, such as small errors in flow density or height of fluid in the reservoir to which the forward model is very sensitive, or microstructural differences in the particle and bubble populations. Yield stress measurements at all bubble fractions show scatter between experiments and misfit to the model higher than the uncertainty predicted by EnKF model fitting, which may come from real variation among samples rather than trade-offs between fitting parameters.

We see consistent deviations between the experimental data and the rheology model in the range of $\phi_{\text{gas}} > 0.6$, where the model consistently over-predicts both the relative consistency and flow index, perhaps due to trade-offs in the inversion of the experimental data. To test the importance of trade-offs in fitting parameters, we find the Pearson correlation coefficients between the EnKF instances after the final propagation (best fit for the fitting parameters) for each experiment. A value of 1 indicates a perfect positive correlation, −1 a perfect negative correlation, and 0 no correlation.The EnKF analyses reveal a moderate correlation between the slope angle and consistency, with an average correlation coefficient between EnKF samples for each experiment of $C = 0.63$. We also find weak correlations between slope angle and yield stress ($C = 0.25$) and slope angle and flow index (C=−0.44); a weak positive correlation between consistency and flow index in experiments with $\phi_{\text{gas}} > 0.6$ ($C = 0.27$); a moderate negative correlation when $\phi_{\text{gas}} < 0.2$ (C=−0.40); and no apparent correlation at intermediate gas volume fractions $0.2 < \phi_{\text{gas}} < 0.6$ ($C = -0.01$). We do not observe correlations in the parameter inversions between yield stress and consistency ($C = -0.06$) or yield stress and flow index ($C = 0.11$). For an example of the EnKF inversion results and match to experimental data see electronic supplementary material, figure S5.

Our results consider strain rates up to $10^1\ \text{s}^{-1}$ and maximum Ca between $\approx 10^{-2}$ and 10^1. We find that bubbles lead to a higher effective viscosity than predicted by the Cross model [1], but our experiments do not cover a large-enough range of Ca to comment on asymptotic behaviour that may occur at much higher or lower Ca. Given the strong strain-rate dependence of the Herschel–Bulkley formulation, this model may not be appropriate for fluids experiencing strain rates far outside the calibration region ($\gg 10\ \text{s}^{-1}$) as may occur in natural settings, including during conduit ascent in explosive eruptions or in fast-moving lava flows.

Additional uncertainty exists for the estimate of Ca, which is difficult to define for a polydisperse bubble population whose exact bubble sizes and deformation cannot be directly observed. Estimates for the bubble size distribution are available in the supplementary material. Bubble deformation is observed for some of the largest bubbles experiencing the strongest shear, and thus experiencing the highest Ca conditions, imaged through the side walls of the channel (electronic supplementary material, figure S2). Such observations are limited to the exterior of the flow, which is necessarily dominated by edge effects. Better characterization of bubble sizes and deformations in the flow interior is an avenue for future work.

(c) Application to lava dynamics

We demonstrate the implications of our new three-phase suspension rheology model with realistic parameters for lava flows through implementation to the channelized lava flow model PyFLOWGO [62,63]. PyFLOWGO is a one-dimensional lava flow advance model for the velocity and final runout distance of a cooling and crystallizing lava. The physical model uses a Bingham-plastic rheology of the form $\tau = \tau_y + \eta_{\text{eff}}\dot{\gamma}$. We add our experimentally constrained rheology

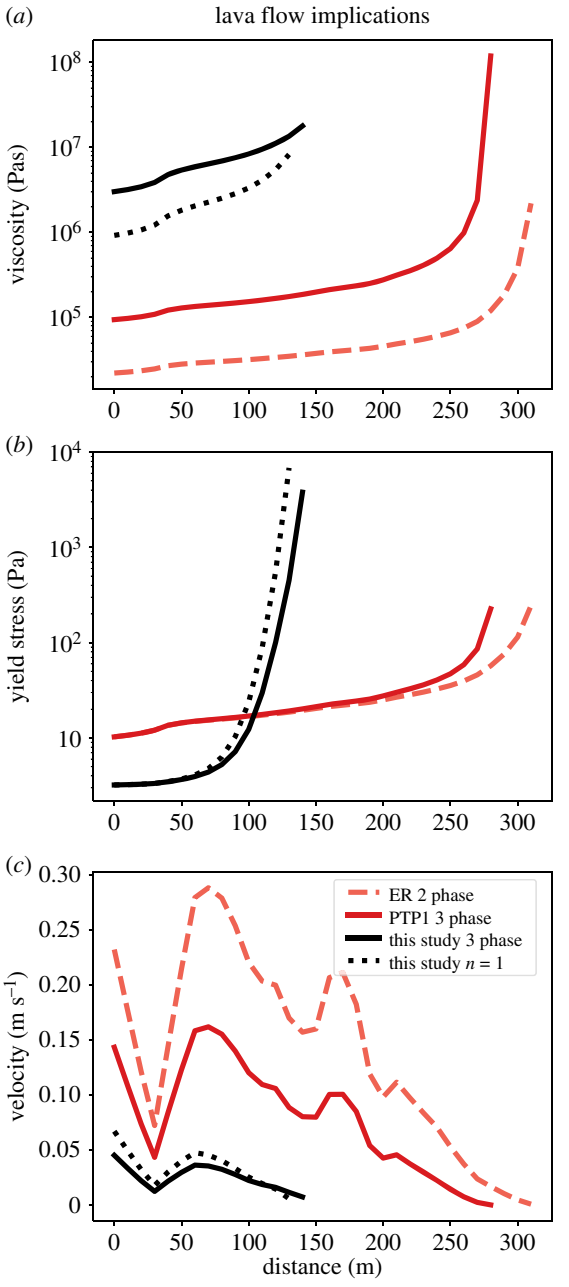

Figure 4. Implications of the experimentally determined three-phase rheology on predictions of lava flows. Our model results in a higher relative effective viscosity (*a*), a sharper increase in yield stress as particle-bubble interactions become important (*b*), and lower mean velocity (*c*) compared to the models of Roscoe [46] (two-phase) or Phan-Thien & Pham [16] (three-phase). We also highlight the contrast between assuming n=1 (Bingham-plastic rheology) and the Herschel–Bulkley rheology ($n\approx0.8$) that results in a decrease in effective viscosity by a factor of 2 at low crystal fractions. (Online version in colour.)

model to several built-in parameterizations for the yield stress and effective viscosity. We calculate τ_y using equation (4.1*b*) and the effective viscosity term $\eta_{\text{eff}} = K_r \mu \dot{\gamma}^{n-1}$ using equations (4.1*a*) and (4.1*c*). We compare our model with the commonly used two-phase modified Einstein–Roscoe relationship [46], and three-phase model of Phan-Thien & Pham [16].

We take the flow simulation parameters from the well-documented LSF1 lava flow from Mount Etna, Italy, in 2001. We initiate the simulated lava with a low solid volume fraction of solid = 0.1. Solid fraction then increases, with further crystallization during emplacement, to $\phi_{solid} = 0.15$ when using our rheological relations, and $\phi_{solid} = 0.3$ for the modified Einstein–Roscoe and Phan-Thien & Pham [16] relationships. Gas fraction begins and remains at $\phi_{gas} = 0.65$. The simulated flow follows the path of steepest descent in the pre-eruptive topography. The initial flux is $20\,m^3\,s^{-1}$. We use a temperature-dependent melt viscosity using the VFT equation ($a = -4.827$, $b = 5997$, $c = -330.3$) [64–66]. We tune the model parameters of initial channel width (set to 40 m) and temperature (set to 1223.15 K) to obtain the observed flow height (10 m) and mean velocity (10^{-3} to $4 \times 10^{-2}\,m\,s^{-1}$) when using our new rheology model. The width and initial temperature are held constant across all simulations. To predict the effective viscosity, we use a reference strain rate of $10^{-3}\,s^{-1}$ for this lava flow, estimated from observed velocities and flow thickness. We approximate the shear rate dependence using the capillary number calculated for a 1 cm radius bubble and a surface tension of air in basalt of $0.37\,N\,m^{-1}$ [29]. As the flow cools, the melt viscosity, crystal content and effective bulk viscosity are updated every step.

Our model predicts a higher effective viscosity compared with that of Phan-Thien & Pham [16] or Roscoe [46] by more than an order of magnitude, and yields a mean velocity that is approximately three times slower (figure 4). Additionally, our yield strength model diverges from that based on Dragoni [67] approximately 80 m down flow, when the crystal fraction increases enough to support significant bubble-crystal interactions. Although shear-thinning behaviour is not included in PyFLOWGO, we compare effective viscosities predicted by our model assuming a Bingham-plastic rheology ($n = 1$) and with a dynamic value for n in response to changing crystal fraction (while maintaining a constant shear rate). We highlight that for the large bubble volume fraction of some natural lavas, n deviates from one (initially $n \approx 0.82$) and can result in a factor of two difference in effective viscosity, and a 15% difference in runout distance. This effect may be more pronounced in modelling that includes a physical model for shear-rate dependence in the flow.

6. Conclusion

We use a dam-break set-up to measure the rheology of three-phase suspensions, scaled to apply to magma and lava. Through the use of a chemical reaction between baking soda and citric acid, we are able to create corn syrup suspensions with bubble volume fractions up to 0.82 and particle volume fractions up to 0.37. Strain rates in our experiments range up to $10\,s^{-1}$ and maximum Ca between $\approx 10^{-2}$ and 10, relevant to basaltic lava flows. We invert for a Herschel–Bulkley rheology using a depth-integrated one-dimensional forward model [39] and the probabilistic ensemble Kalman filter approach.

Based on our results, we develop a suite of models for the Herschel–Bulkeley parameters, calibrated across the whole dataset, which are presented in equations (4.1*a*)–(4.1*c*). Combined with equation (2.3), this constitutes a rheological model for three-phase suspensions. Our results show good agreement with existing literature for particle-bearing suspensions with a strongly nonlinear increase in viscosity with increasing particle fraction, development of yield stresses at particle fractions $\phi_{solid} \gtrsim 0.35$, and development of shear-thinning behaviour at particle fractions $\phi_{solid} \gtrsim 0.39$. Our findings indicate that suspended gas leads to a nonlinear increase in viscosity with increasing bubble fraction, larger than predicted by previous work, and development of yield stresses and shear rate-dependent behaviour at bubble fractions, or combined bubble and particle fractions, similar to those observed for particle-only suspensions. We find that shear-rate dependence of bubble-bearing two- and three-phase suspensions are shear thinning in the low capillary number regime and become shear thickening with increasing capillary number. This study contributes an explicit incorporation of three-phase interactions into a novel model for yield stress, and a parameterization for the inclusion of capillary number in flow index.

We highlight the implications of our model for magma/lava dynamics through application to the lava flow emplacement model PyFLOWGO, and show higher viscosities and lower predicted velocities for surface lava flows as a result of the stiffening behaviour of concentrated bubble suspensions at low and intermediate capillary numbers. Our findings underscore the need to incorporate three-phase rheology into simulations of magma or lava flow used to address fundamental science questions as well as hazard assessment and mitigation.

Data accessibility. Experiment videos available at https://doi.org/10.5281/zenodo.4685257. data processing code available at https://doi.org/10.5281/zenodo.4707969 or https://github.com/JanineBirnbaum18/3-phase-flow.

Authors' contributions. J.B. carried out the experiments and data analysis. E.L. conceived of and supervised the experiments and data analysis. E.W.L. contributed to the interpretation of the results. J.B. took the lead in writing the manuscript. All authors provided critical feedback and helped shape the research, analysis and manuscript.

Competing interests. The authors have no competing interests to declare.

Funding. This work was supported by NSF under awards NSF EAR-1654588 and NSF EAR-1929008, and by NERC under award NE/T009594/1.

Acknowledgements. We thank J. Hammer and A. Whittington for their constructive comments, and Lamont-Doherty's Secondary School Field Research Program participants R. Burgos, M. Diakite and L. Lyons for their assistance in conducting experiments. We thank two anonymous reviewers for their constructive suggestions which helped improve and clarify the manuscript.

References

1. Mader HM, Llewellin EW, Mueller SP. 2013 The rheology of two-phase magmas: a review and analysis. *J. Volcanol. Geotherm. Res.* **257**, 135–158. (doi:10.1016/j.jvolgeores.2013.02.014)
2. Einstein A. 1911 Berichtigung zu meiner Arbeit: Eine neue Bestimmung der Moleküldimensionen. *Annalen der Physik* **339**, 591–592. (doi:10.1002/andp.19113390313)
3. Krieger IM, Dougherty TJ. 1959 A mechanism for non–Newtonian flow in suspensions of rigid spheres. *Trans. Soc. Rheol.* **3**, 137–152. (doi:10.1122/1.548848)
4. Mueller S, Llewellin EW, Mader HM. 2010 The rheology of suspensions of solid particles. *Proc. R. Soc. A* **466**, 1201–1228. (doi:10.1007/BF01432034)
5. Chesterton AKS, De Abreu DAP, Moggridge GD, Sadd PA, Wilson DI. 2013 Evolution of cake batter bubble structure and rheology during planetary mixing. *Food Bioprod. Process.* **91**, 192–206. (doi:10.1016/j.fbp.2012.09.005)
6. Llewellin EW, Mader HM, Wilson SDR. 2002 The constitutive equation and flow dynamics of bubbly magmas. *Geophys. Res. Lett.* **29**, 1–4. (doi:10.1029/2002gl015697)
7. Llewellin EW, Manga M. 2005 Bubble suspension rheology and implications for conduit flow. *J. Volcanol. Geotherm. Res.* **143**, 205–217. (doi:10.1016/j.jvolgeores.2004.09.018)
8. Manga M, Castro J, Cashman KV, Loewenberg M. 1998 Rheology of bubble-bearing magmas. *J. Volcanol. Geotherm. Res.* **87**, 15–28. (doi:10.1016/S0012-821X(98)00278-7)
9. Pal R. 2003 Rheological behavior of bubble-bearing magmas. *Earth Planet. Sci. Lett.* **207**, 165–179. (doi:10.1016/S0012-821X(02)01104-4)
10. Pistone M, Caricchi L, Ulmer P, Burlini L, Ardia P, Reusser E, Marone F, Arbaret L. 2012 Deformation experiments of bubble- and crystal-bearing magmas: Rheological and microstructural analysis. *J. Geophys. Res.* **117**, 1–39. (doi:10.1029/2011JB008986)
11. Princen HM, Kiss AD. 1989 Rheology of foams and highly concentrated emulsions: IV. An experimental study of the shear viscosity and yield stress of concentrated emulsions. *J. Colloid Interface Sci.* **128**, 176–187. (doi:10.1016/j.cocis.2014.11.003)
12. Rouyer F, Cohen-Addad S, Höhler R. 2005 Is the yield stress of aqueous foam a well-defined quantity? *Colloids Surf. A* **263**, 111–116. (doi:10.1016/j.colsurfa.2005.01.025)
13. Rust AC, Manga Michael. 2002 Effects of bubble deformation on the viscosity of dilute suspensions. *J. Non-Newtonian Fluid Mech.* **104**, 53–63. (doi:10.1016/S0377-0257(02)00013-7)
14. Stein DJ, Spera FJ. 1992 Rheology and microstructure of magmatic emulsions: theory and experiments. *J. Volcanol. Geotherm. Res.* **49**, 157–174. (doi:10.1016/0377-0273(92)90011-2)
15. Taylor GI. 1932 The viscosity of a fluid containing small drops of another fluid. *Proc. R. Soc. Lond. A* **138**, 41–48. (doi:10.1098/rspa.1932.0169)

16. Phan-Thien N, Pham DC. 1997 Differential multiphase models for polydispersed suspensions and particulate solids. *J. Non-Newtonian Fluid Mech.* **72**, 305–318. (doi:10.1016/S0377-0257(97)90002-1)
17. Truby JM, Mueller SP, Llewellin EW, Mader HM. 2015 The rheology of three-phase suspensions at low bubble capillary number. *Proc. R. Soc. A* **471**, 1–18. (doi:10.1098/rspa.2014.0557)
18. Dingwell DB, Webb SL. 1989 Structural relaxation in silicate melts and non-Newtonian melt rheology in geologic processes. *Phys. Chem. Miner.* **16**, 508–516. (doi:10.1007/BF00197020)
19. Giordano D, Russell JK, Dingwell DB. 2008 Viscosity of magmatic liquids: a model. *Earth Planet. Sci. Lett.* **271**, 123–134. (doi:10.1016/j.epsl.2008.03.038)
20. Gonnermann HM, Manga M. 2007 The fluid mechanics inside a volcano. *Annu. Rev. Fluid Mech.* **39**, 321–356. (doi:10.1146/annurev.fluid.39.050905.110207)
21. Cashman KV, Stephen R, Sparks J. 2013 How volcanoes work: a 25 year perspective. *Bull. Geol. Soc. Am.* **125**, 664–690. (doi:10.1130/B30720.1)
22. Ryerson FJ, Weed HC, Piwinskii AJ. 1988 Rheology of subliquidus magmas. 1. Picritic compositions. *J. Geophys. Res.* **93**, 3421–3436. (doi:10.1029/JB093iB04p03421)
23. Pinkerton H, Norton G. 1995 Rheological properties of basaltic lavas at sub-liquidus temperatures: laboratory and field measurements on lavas from Mount Etna. *J. Volcanol. Geotherm. Res.* **68**, 307–323. (doi:10.1016/0377-0273(95)00018-7)
24. Ishibashi H. 2009 Non-Newtonian behavior of plagioclase-bearing basaltic magma: subliquidus viscosity measurement of the 1707 basalt of Fuji volcano, Japan. *J. Volcanol. Geotherm. Res.* **181**, 78–88. (doi:10.1016/j.jvolgeores.2009.01.004)
25. Soldati A, Sehlke A, Chigna G, Whittington A. 2016 Field and experimental constraints on the rheology of arc basaltic lavas: the January 2014 Eruption of Pacaya (Guatemala). *Bull. Volcanol.* **78**, 1–19. (doi:10.1007/s00445-016-1031-6)
26. Castruccio A, Rust AC, Sparks RSJ. 2010 Rheology and flow of crystal-bearing lavas: insights from analogue gravity currents. *Earth Planet. Sci. Lett.* **297**, 471–480. (doi:10.1016/j.epsl.2010.06.051)
27. Bagdassarov N, Dorfman A, Dingwell DB. 2000 Effect of alkalis, phosphorus, and water on the surface tension of haplogranite melt. *Am. Mineral.* **85**, 33–40. (doi:10.2138/am-2000-0105)
28. Mangan M, Sisson T. 2005 Evolution of melt-vapor surface tension in silicic volcanic systems: experiments with hydrous melts. *J. Geophys. Res.: Solid Earth* **110**, 1–9. (doi:10.1029/2004JB003215)
29. Walker D, Mullins O. 1981 Surface tension of natural silicate melts from 1200° − 1500°C and implications for melt structure. *Contrib. Mineral. Petrol.* **76**, 455–462. (doi:10.1007/BF00371487)
30. Petford N, Koenders MA, Clemens JD. 2020 Igneous differentiation by deformation. *Contrib. Mineral. Petrol.* **175**, 1–21. (doi:10.1007/s00410-020-1674-3)
31. Vergniolle S. 1996 Bubble size distribution in magma chambers and dynamics of basaltic eruptions. *Earth Planet. Sci. Lett.* **140**, 269–279. (doi:10.1016/0012-821X(96)00042-8)
32. Galindo I, Gudmundsson A. 2012 Basaltic feeder dykes in rift zones: geometry, emplacement, and effusion rates. *Nat. Hazards Earth Syst. Sci.* **12**, 3683–3700. (doi:10.5194/nhess-12-3683-2012)
33. Gaonac'h H, Lovejoy S, Schertzer D. 2005 Scaling vesicle distributions and volcanic eruptions. *Bull. Volcanol.* **67**, 350–357. (doi:10.1007/s00445-004-0376-4)
34. Thivet S, Gurioli L, Di Muro A. 2020 Basaltic dyke eruptions at Piton de La Fournaise: characterization of the eruptive products with implications for reservoir conditions, conduit processes and eruptive dynamics. *Contrib. Mineral. Petrol.* **175**, 1–24. (doi:10.1007/s00410-020-1664-5)
35. Petcovic HL, Dufek JD. 2005 Modeling magma flow and cooling in dikes: implications for emplacement of Columbia River flood basalts. *J. Geophys. Res.: Solid Earth* **110**, 1–15. (doi:10.1029/2004JB003432)
36. Herschel WH, Bulkley R. 1926 Konsistenzmessungen von Gummi-Benzollösungen. *Kolloid Zeitschrift* **39**, 291. (doi:10.1007/BF01432034)
37. Rust AC, Manga M. 2002 Bubble shapes and orientations in low Re simple shear flow. *J. Colloid Interface Sci.* **249**, 476–480. (doi:10.1006/jcis.2002.8292)
38. Sinat-Radchenko DE. 1982 Surface tension of sugar solutions. *Sakharnaia Promyshlennost* **3**, 28–31.
39. Liu KF, Mei CC. 1989 Slow spreading of a sheet of Bingham fluid on an inclined plane. *J. Fluid Mech.* **207**, 505–529. (doi:10.1017/S0022112089002685)

40. Balmforth NJ, Craster RV, Perona P, Rust AC, Sassi R. 2007 Viscoplastic dam breaks and the Bostwick consistometer. *J. Non-Newtonian Fluid Mech.* **142**, 63–78. (doi:10.1016/j.jnnfm.2006.06.005)
41. Madlener K, Frey B, Ciezki HK. 2009 Generalized Reynolds number for non-Newtonian fluids. *Progress Propulsion Phys.* **1**, 237–250. (doi:10.1051/eucass/200901237)
42. de Gennes P-G, Brochard-Wyart F, Quéré D. 2004 *Capillarity and wetting phenomena*. New York, NY: Springer.
43. Gregg PM, Pettijohn JC. 2016 A multi-data stream assimilation framework for the assessment of volcanic unrest. *J. Volcanol. Geotherm. Res.* **309**, 63–77. (doi:10.1016/j.jvolgeores.2015.11.008)
44. Zhan Y, Gregg PM. 2017 Data assimilation strategies for volcano geodesy. *J. Volcanol. Geotherm. Res.* **344**, 13–25. (doi:10.1016/j.jvolgeores.2017.02.015)
45. Byrd RH, Lu P, Nocedal J. 1995 A limited memory algorithm for bound constrained optimization. *SIAM J. Sci. Stat. Comput.* **16**, 1190–1208. (doi:10.1137/0916069)
46. Roscoe R. 1952 The viscosity of suspensions of rigid spheres. *Br. J. Appl. Phys.* **3**, 267–269. (doi:10.1088/0508-3443/3/8/306)
47. Mooney M. 1951 The viscosity of a concentrated suspension of spherical particles. *J. Colloid Sci.* **6**, 162–170. (doi:10.1016/0095-8522(51)90036-0)
48. Costa A, Caricchi L, Bagdassarov N. 2009 A model for the rheology of particle-bearing suspensions and partially molten rocks. *Geochem. Geophys. Geosyst.* **10**, 1–13. (doi:10.1029/2008GC002138)
49. Hoover SR, Cashman KV, Manga M. 2001 The yield strength of subliquidus basalts - experimental results. *J. Volcanol. Geotherm. Res.* **107**, 1–18. (doi:10.1016/S0377-0273(00)00317-6)
50. Coussot P. 2014 Yield stress fluid flows: a review of experimental data. *J. Non-Newtonian Fluid Mech.* **211**, 31–49. (doi:10.1016/j.jnnfm.2014.05.006)
51. Hogg AJ, Matson GP. 2009 Slumps of viscoplastic fluids on slopes. *J. Non-Newtonian Fluid Mech.* **158**, 101–112. (doi:10.1016/j.jnnfm.2008.07.003)
52. Ancey C, Cochard S. 2009 The dam-break problem for Herschel-Bulkley viscoplastic fluids down steep flumes. *J. Non-Newtonian Fluid Mech.* **158**, 18–35. (doi:10.1016/j.jnnfm.2008.08.008)
53. Huang X, García MH. 1998 A Herschel-Bulkley model for mud flow down a slope. *J. Fluid Mech.* **374**, 305–333. (doi:10.1017/S0022112098002845)
54. Vola D, Babik F, Latché JC. 2004 On a numerical strategy to compute gravity currents of non-Newtonian fluids. *J. Comput. Phys.* **201**, 397–420. (doi:10.1016/j.jcp.2004.05.019)
55. Ancey C, Andreini N, Epely-Chauvin G. 2012 Viscoplastic dambreak waves: review of simple computational approaches and comparison with experiments. *Adv. Water Res.* **48**, 79–91. (doi:10.1016/j.advwatres.2012.03.015)
56. Andreini N, Epely-Chauvin G, Ancey C. 2012 Internal dynamics of Newtonian and viscoplastic fluid avalanches down a sloping bed. *Phys. Fluids* **24**, 1–20. (doi:10.1063/1.4718018)
57. Cantelli A. 2009 Uniform flow of modified Bingham fluids in narrow cross sections. *J. Hydraulic Eng.* **135**, 640–650. (doi:10.1061/(asce)hy.1943-7900.0000092)
58. Chambon G, Ghemmour A, Naaim M. 2014 Experimental investigation of viscoplastic free-surface flows in a steady uniform regime. *J. Fluid Mech.* **754**, 332–364. (doi:10.1017/jfm.2014.378)
59. Cochard S, Ancey C. 2009 Experimental investigation of the spreading of viscoplastic fluids on inclined planes. *J. Non-Newtonian Fluid Mech.* **158**, 73–84. (doi:10.1016/j.jnnfm.2008.08.007)
60. Longo S, Chiapponi L, Di Federico V. 2016 On the propagation of viscous gravity currents of non-Newtonian fluids in channels with varying cross section and inclination. *J. Non-Newtonian Fluid Mech.* **235**, 95–108. (doi:10.1016/j.jnnfm.2016.07.007)
61. Boujlel J, Maillard M, Lindner A, Ovarlez G, Chateau X, Coussot P. 2012 Boundary layer in pastes–displacement of a long object through a yield stress fluid. *J. Rheol.* **56**, 1083–1108. (doi:10.1122/1.4720387)
62. Harris AJL, Rowland Scott K. 2001 FLOWGO: a kinematic thermo-rheological model for lava cooling in a channel.
63. Chevrel MO, Labroquère J, Harris AJL, Rowland SK. 2018 PyFLOWGO: an open-source platform for simulation of channelized lava thermo-rheological properties. *Comput. Geosci.* **111**, 167–180. (doi:10.1016/j.cageo.2017.11.009)
64. Cordonnier B, Lev E, Garel F. 2016 Benchmarking lava-flow models. *Geol. Soc. Lond.* **426**, 425–445. (doi:10.1144/SP426.7)

65. Coltelli M, Proietti C, Branca S, Marsella Maria, Andronico D, Lodato L. 2007 Analysis of the 2001 lava flow eruption of Mt. Etna from three-dimensional mapping. *J. Geophys. Res.: Earth Surface* **112**, 1–18. (doi:10.1029/2006JF000598)
66. Lombardo V, Buongiorno MF. 2006 Lava flow thermal analysis using three infrared bands of remote-sensing imagery: a study case from Mount Etna 2001 eruption. *Remote Sens. Environ.* **101**, 141–149. (doi:10.1016/j.rse.2005.12.008)
67. Dragoni M. 1989 A dynamical model of lava flows cooling by radiation. *Bull. Volcanol.* **51**, 88–95. (doi:10.1007/BF01081978)